Quantum correlations between light and the kilogram-mass mirrors of LIGO

https://doi.org/10.1038/s41586-020-2420-8

Received: 3 February 2020

Accepted: 4 May 2020

Published online: 1 July 2020

Check for updates

Haocun Yu[1]✉, L. McCuller[1]✉, M. Tse[1], N. Kijbunchoo[2], L. Barsotti[1], N. Mavalvala[1] and other members of the LIGO Scientific Collaboration*

The measurement of minuscule forces and displacements with ever greater precision is inhibited by the Heisenberg uncertainty principle, which imposes a limit to the precision with which the position of an object can be measured continuously, known as the standard quantum limit[1–4]. When light is used as the probe, the standard quantum limit arises from the balance between the uncertainties of the photon radiation pressure applied to the object and of the photon number in the photoelectric detection. The only way to surpass the standard quantum limit is by introducing correlations between the position/momentum uncertainty of the object and the photon number/phase uncertainty of the light that it reflects[5]. Here we confirm experimentally the theoretical prediction[5] that this type of quantum correlation is naturally produced in the Laser Interferometer Gravitational-wave Observatory (LIGO). We characterize and compare noise spectra taken without squeezing and with squeezed vacuum states injected at varying quadrature angles. After subtracting classical noise, our measurements show that the quantum mechanical uncertainties in the phases of the 200-kilowatt laser beams and in the positions of the 40-kilogram mirrors of the Advanced LIGO detectors yield a joint quantum uncertainty that is a factor of 1.4 (3 decibels) below the standard quantum limit. We anticipate that the use of quantum correlations will improve not only the observation of gravitational waves, but also more broadly future quantum noise-limited measurements.

The Heisenberg uncertainty principle dictates that once an object is localized with sufficient precision, the momentum of that object must become accordingly uncertain. In a one-off measurement, this does not pose a problem. However, when the position of an object must be measured continuously, as in gravitational wave (GW) detectors, the momentum uncertainty introduced by the act of measuring the position evolves into a position uncertainty for future position measurements—a process known as quantum backaction. In striking a balance between the precision of position measurements and the imprecision caused by quantum backaction, an apparent maximum precision is reached for a continuous position measurement. This is the standard quantum limit (SQL), and for an interferometric measurement, as long as the shot noise and quantum radiation pressure noise (QRPN) are uncorrelated, the SQL is indeed the limit.

The SQL was first introduced by Braginsky et al.[2,3] as a fundamental limit to the sensitivity of GW detectors. It should be possible to reach the SQL with objects that are macroscopic or even human-scale because the quantization of the probe light is what enforces the SQL (see, for example, footnote 1 of ref. [4]). In principle, the SQL can be surpassed when the shot noise and the QRPN are correlated. Such correlations already exist in the interferometer because incoming quantum fluctuations entering from its output port drive both the shot noise and the QRPN, giving rise to ponderomotive squeezing. An injected squeezed state, when combined appropriately with ponderomotive squeezing, enables surpassing the SQL (see section IVB of ref. [4]). Alternative methods for surpassing the SQL in GW detectors are presented in refs. [4,6].

Here, we inject a laser mode that is in a squeezed vacuum state into a laser interferometric GW detector with 40-kg mirrors, and use the optomechanically induced correlations of ponderomotive squeezing to demonstrate quantum noise below the SQL. This measurement marks two milestones of quantum measurement. First, we directly observe the contribution of the QRPN to the motion of kilogram-mass objects at room temperature, indicating that quantum backaction imposed by the Heisenberg uncertainty principle persists even at human scales. Second, we demonstrate quantum noise below the SQL, proving the existence of quantum correlations involving the position uncertainty of the 40-kg mirrors. This measurement is an important step towards further improvements in GW sensitivity through quantum engineering techniques[4,6–10].

A considerable barrier to revealing quantum correlations between light and macroscopic objects is the ubiquitous presence of thermal fluctuations that drive their motion. Previous demonstrations of the QRPN have involved cryogenically precooled pico- to microgram-scale mechanics[10–14], with three exceptions[15–17]. Similarly, a previous sub-SQL measurement of displacement was performed on a cryogenically precooled mechanical oscillator at the nanogram

[1]LIGO, Massachusetts Institute of Technology, Cambridge, MA, USA. [2]OzGrav, Australian National University, Canberra, Australian Capital Territory, Australia. *A list of authors and their affiliations appears at the end of the paper. ✉e-mail: haocunyu@mit.edu; mcculler@mit.edu

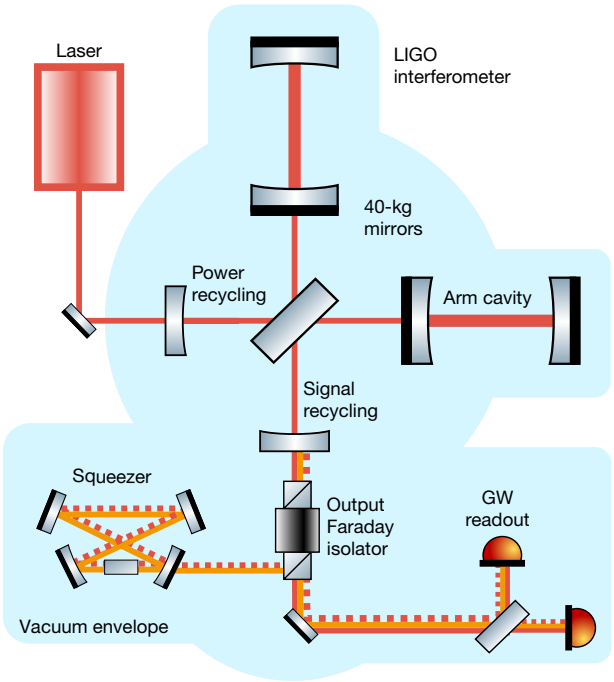

Fig. 1 | Simplified schematic of the experimental setup. Squeezed vacuum (dashed red line) is injected through the output Faraday isolator and co-propagates with the 1,064-nm light (solid red line) of the main interferometer. A frequency-shifted control field (orange line) is used to sense the squeeze angle and control it using the phase of the squeezer pump field (not shown)[19].

mass scale[18]. The measurements presented here are performed on the room-temperature, 40-kg mirrors of Advanced LIGO using laser light of 200 kW, and are enabled by the injection of squeezed states and sufficiently low classical noise. The classical noise is subtracted to reveal quantum noise below the SQL.

We performed this experiment using the Advanced LIGO detector in Livingston, Louisiana, USA. For the third astrophysics observing run of LIGO/Virgo, squeezed vacuum is injected into the interferometer, with the squeezing level and squeezing quadrature angle tuned to maximize the GW sensitivity[19]. In this experiment, the interferometer is maintained in the observing configuration, but data are taken with an increased squeezing level and over a range of squeezing angles in order to fully characterize the quantum noise.

The Advanced LIGO detector is a Michelson interferometer with two 4-km Fabry–Pérot arms, as well as power- and signal-recycling cavities at the input and output ports of the beam splitter, respectively (see Fig. 1). The arm-cavity optics are 40-kg fused-silica mirrors, suspended as pendulums inside an ultrahigh-vacuum envelope[20]. During the measurement, 200 ± 10 kW of 1,064-nm laser power circulates in each arm cavity. The differential arm displacement signal (Δx) is detected as modulations of a small static field at the GW readout caused by a deliberate mismatch in the interferometer arm lengths[20]. The displacement signal Δx is part of a closed servo loop, which is monitored by a continuous calibration procedure that also extracts the instrument sensing function by driving the differential arm motion and measuring the optical response. Details of the squeezed light source and its operation, including the control method for adjusting the squeezing angle, are provided in ref. [19]. For this measurement, injected squeezing results in 3.3 dB of squeezing and 7.7 dB of antisqueezing measured at the GW readout.

An analytic model of the displacement sensitivity in an ideal LIGO interferometer illustrates how the combination of ponderomotive squeezing and injected squeezing allows us to surpass the SQL for the differential arm motion. A model that builds on methods developed in refs. [4,6], with extensions to account for losses and off-resonance cavities, is provided in Methods. Here, the ideal model is used for clarity. The application of the Heisenberg uncertainty principle to an interferometric measurement of differential displacement Δx sets a limit to the one-sided spectral density of:

$$\Delta x^2(\Omega) = S(\Omega,\phi)[1+\mathcal{K}^2(\Omega)]\frac{\hbar c}{8k|G(\Omega)|^2 P_{\mathrm{arm}}} \quad (1)$$

with

$$\mathcal{K}(\Omega) = \frac{32k|G(\Omega)|^2 P_{\mathrm{arm}}}{m\Omega^2 c},\ G(\Omega) \equiv \sqrt{\frac{\gamma c}{2L}}\frac{1}{\gamma + \mathrm{i}\Omega}. \quad (2)$$

Here P_{arm} is the circulating arm power; k is the laser wavenumber; $\Omega/(2\pi)$ is the sideband frequency of the GW readout; m is the mass of each mirror; $\hbar$ is the reduced Planck constant; L is the arm length of 3,995 m; and γ is the signal bandwidth of $2\pi \times 450$ Hz in LIGO. $G(\Omega)$ is the optical-field transmissivity between the arm cavities and the readout detector, making $2kG(\Omega)\sqrt{P_{\mathrm{arm}}}$ the sensing function that relates Δx to the emitted optical field that modulates the GW readout power.

The factors $S(\Omega,\phi)$ and $1+\mathcal{K}^2(\Omega)$ (ϕ, squeeze angle) capture the radiation pressure interaction, whereby the mirror oscillator motion correlates the injected optical amplitude quadrature to the output phase quadrature, with $\mathcal{K}(\Omega)$ the ponderomotive interaction strength. The theory of ponderomotive squeezing is detailed in section IVA-B of ref. [4]. $S(\Omega,\phi)$ accounts for the injection of squeezed states. Without injected squeezing, $S=1$, in which case the arm power P_{arm} may be chosen to minimize $\Delta x(\Omega)$ by balancing the shot noise and the radiation pressure noise. The resulting minimum $\Delta x_{\mathrm{SQL}}(\Omega)$ is the free-mass SQL for a Michelson interferometer with a Fabry–Pérot cavity in each arm[4]:

$$\Delta x^2(\Omega) \geq \Delta x^2_{\mathrm{SQL}}(\Omega) \equiv \frac{8\hbar}{m\Omega^2}. \quad (3)$$

When injecting squeezed states at a squeeze angle ϕ with a squeeze factor r, the squeezing measured at the readout, $S(\Omega,\phi)$, becomes:

$$S(\Omega,\phi) = \mathrm{e}^{-2r}\cos^2[\phi-\theta(\Omega)] + \mathrm{e}^{2r}\sin^2[\phi-\theta(\Omega)] \quad (4)$$

$$\theta(\Omega) = \arctan[\mathcal{K}(\Omega)]. \quad (5)$$

$\phi = 0$ is defined as the squeezing angle that reduces the power spectral density of the shot noise, where $\theta \to 0$, by a factor of e^{-2r}.

The expression $\phi - \theta(\Omega)$ characterizes the frequency-dependent interaction between ponderomotive and injected squeezing. Equation (4) indicates that at frequencies for which $\theta(\Omega) = \phi$, these two combine to produce a minimum in the quantum noise spectrum, which appears as a 'dip' in the curves of Fig. 2. Whereas the $S=1$ case led to the SQL in equation (3), injecting squeezed states allows the SQL to be surpassed at measurement frequencies for which $S(\Omega,\phi) < 1$.

Figure 2 shows amplitude spectral densities of differential displacement. Exposing the sub-SQL dip requires reliably estimating and subtracting classical noise around 40 Hz. The data are acquired as three sets of spectral measurements in each of two operating modes: with and without squeezing injection. By alternating operation between the two modes, we establish that the noise is consistent within statistical variations, confirming that it is stationary over the duration of the experiment. To further address the concern that the classical noise between modes of operation may be changing, additional data at a range of squeezing angles are obtained, as shown in Fig. 3.

In Fig. 2, the black trace is the measured total noise at the readout with squeezing disengaged, including both quantum and classical noise

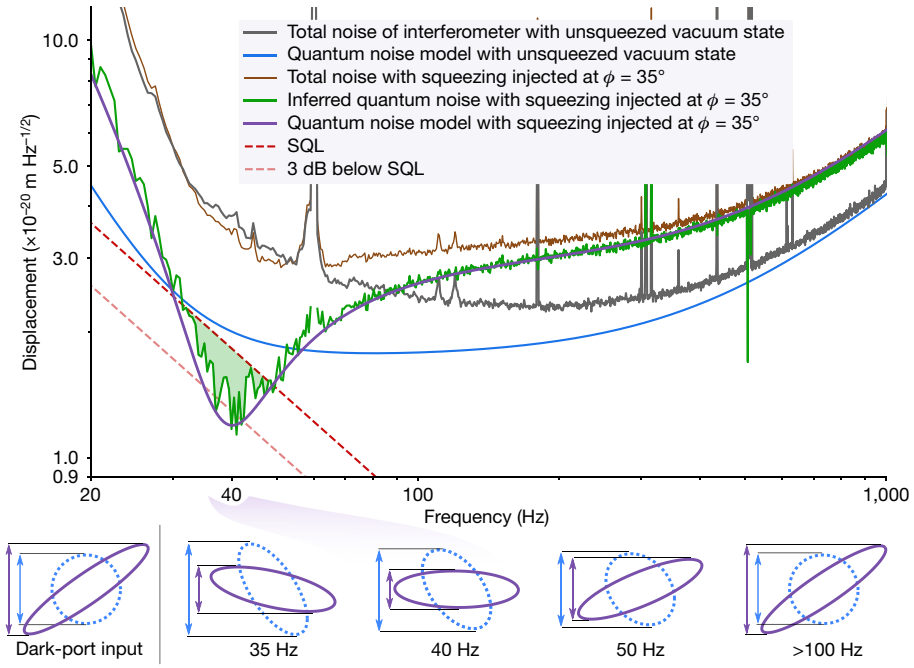

Fig. 2 | Spectral density measurements revealing sub-SQL quantum noise. Top, spectral density of the differential displacement (Δx) noise of the interferometer. The grey and brown traces show the measured total noise level of the interferometer with the unsqueezed vacuum state (that is, the reference) and injected squeezing at 35°, respectively. The blue trace is the model of quantum noise during the reference measurement. The green trace shows the inferred quantum noise of the interferometer with injected squeezing at 35°, and its corresponding model is the purple trace. The notch feature, or 'dip', results from the ponderomotive squeezing affecting the injected optical squeezed states. It reaches −3 dB of the free-mass SQL (red dashed trace; given by equation (3)) at 40 Hz. Bottom, phase-space representation of the modelled quantum states entering through the dark port of the interferometer (left) and the output states (right), with their frequency dependence indicated. Shown are the cases in which the input state is unsqueezed vacuum (dashed blue line) and squeezing at ϕ = 35° (solid purple line). In the unsqueezed vacuum case, ponderomotive squeezing distorts the ellipse for frequencies below 100 Hz, increasing the QRPN in the readout quadrature (blue arrows). In the case of injected squeezing, the same physical process creates a state with reduced noise at 40 Hz (purple arrows).

contributions. It is generated from a 90-min average split across three non-contiguous time periods in which the squeezer cavity is set to be off resonance[19], allowing the unsqueezed vacuum state to enter the interferometer. The blue trace is the modelled quantum noise contribution to the total noise measurement of the black trace. Subtracting the blue trace from the black trace gives the total classical noise contribution. We verify that this classical noise component is stationary and independent of squeezer status (see discussion in the caption of Fig. 3 and details in Methods). The model shows that quantum noise dominates the interferometer sensitivity at high frequencies ($\Omega > \gamma \approx 2\pi \times 450$ Hz), and accounts for 28% of the total measured noise power at 40 Hz. Of the remaining non-quantum noise, 24% is estimated to be coating and thermo-optic noise, with the rest unidentified (A. Buikema et al., manuscript in preparation).

The green trace in Fig. 2 shows the inferred quantum noise spectrum with squeezing injected at ϕ = 35°. This angle, determined from the model fit, places the dip in the frequency region in which the ratio between the total measured reference noise and the SQL curve is minimized. The green trace is calculated as the total measured displacement spectrum while the squeezer is engaged (brown trace), minus the classical noise contribution determined from the reference measurement. The purple trace shows the quantum noise model corresponding to ϕ = 35° squeezing, featuring a dip in the quantum noise that reaches down to 70% or 3 dB of the SQL at 40 Hz.

Squeezing measurements at three additional ϕ values are presented in Fig. 3. They show that the QRPN contributes to the motion of the Advanced LIGO mirrors. At each ϕ, the quantum noise trace is calculated by subtracting the same classical noise contribution (determined

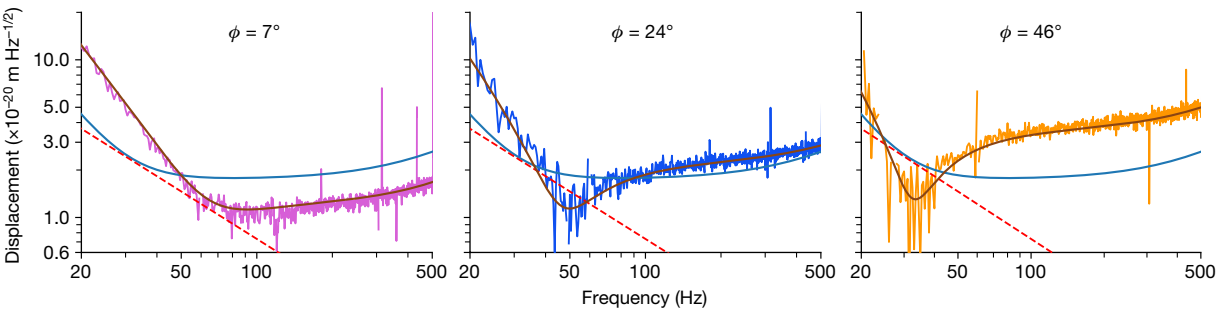

Fig. 3 | Quantum noise spectra at additional squeezing angles of 7°, 24° and 46°. Each dataset is plotted with the same classical noise subtraction as Fig. 2, and with a corresponding quantum noise model curve (copper line). The model without injected squeezing (blue line) is plotted for comparison. The differences between the squeezed datasets and the reference model show that the QRPN contributes to the motion of the Advanced LIGO mirrors. The QRPN contribution can be increased and decreased as the injected state is varied. These data were obtained with less observing time than Fig. 2 and have correspondingly larger statistical fluctuations.

from the reference data) from the measured displacement spectrum. We note that the modelled quantum noise plotted here requires the full functional form of $S(\Omega, \phi, \psi)$ in equation (9) in Methods, rather than the simplified version of equation (4). A total of 12 squeezing measurements are combined to plot $S(\Omega, \phi, \psi)$ in Extended Data Fig. 2.

The uncertainties in both the data and the model are discussed here, with additional details in Methods. The statistical error in the power spectrum measurement of the quantum noise, after subtraction, is 8% at 40 Hz (for a bin width of 0.5 Hz). We test for discrepancies between the three reference datasets and find that the relative uncertainty in the classical noise stationarity is bounded by the same statistical error. Errors in the optical sensing function $2kG(\Omega)\sqrt{P_{\mathrm{arm}}}$, along with the Δx servo loop compensation, are determined from the online interferometer calibration procedure[21] to be ±3%. The uncertainty in the arm-cavity power is 5%. Aside from the reference datasets, the model curves of Figs. 2, 3 require the squeeze factor r and the interferometer losses[19], which are determined from fits across all datasets. The 12 measurements also constrain an additional unwanted frequency-dependent squeezing phase shift of $\psi = 8°$, which accumulates across the frequency region where $\Omega \approx \gamma$. This effect arises from a detuning of the signal-recycling cavity, which is detailed in the Methods, equation (10).

The measurements presented here represent long-awaited milestones in verifying the role of quantum mechanics in limiting the precision of position measurements even for macroscopic objects, and thereby limiting the sensitivity of GW detectors.

First, we observe that the QRPN contributes to the motion of the kilogram-scale mirrors of LIGO. This observation is also made with the Advanced Virgo GW detector (F. Acernese et al., manuscript in preparation). It is remarkable that quantum vacuum fluctuations can influence the motion of these macroscopic, human-scale objects, and that the effect is measured—this is experimental quantum mechanics at its most macroscopic scale.

Second, revealing quantum noise below the SQL in the Advanced LIGO detector is the first realization of a quantum non-demolition technique in GW detectors[2,3], where quantum correlations prevent the measurement device from demolishing the same information that one is trying to extract. Exploiting quantum correlations allows a fundamental quantum limit to be manipulated to improve measurement precision.

Finally, we must not forget the foremost scientific objectives of the Advanced LIGO detectors: they are designed for astrophysical observations of GWs from violent cosmic events. During the third observing run of LIGO/Virgo, the squeezing angle in LIGO is set to optimize the sensitivity of the detectors to GWs from binary neutron star mergers[19]. This is not the squeeze angle at which shot noise is minimized, but that for which the combination of shot noise and QRPN are minimized, implying that backaction evasion plays a role in optimizing the sensitivity of the Advanced LIGO detector. This is one of the factors that has allowed Advanced LIGO to go from detecting roughly one astrophysical event per month in observing runs 1 and 2, to about one astrophysical trigger per week in the third observing run of LIGO/Virgo. With further mitigation of classical noise, the sub-SQL performance of GW detectors promises ever greater astrophysical reach in the future.

Online content

Any methods, additional references, Nature Research reporting summaries, source data, extended data, supplementary information, acknowledgements, peer review information; details of author contributions and competing interests; and statements of data and code availability are available at https://doi.org/10.1038/s41586-020-2420-8.

1. Caves, C. M. Quantum-mechanical noise in an interferometer. *Phys. Rev. D* **23**, 1693–1708 (1981).
2. Braginsky, V. B. & Khalili, F. Y. Quantum nondemolition measurements: the route from toys to tools. *Rev. Mod. Phys.* **68**, 1–11 (1996).
3. Braginsky, V. B., Khalili, F. Y. & Thorne, K. S. *Quantum Measurement* (Cambridge University Press, 1992).
4. Kimble, H. J., Levin, Y., Matsko, A. B., Thorne, K. S. & Vyatchanin, S. P. Conversion of conventional gravitational-wave interferometers into quantum nondemolition interferometers by modifying their input and/or output optics. *Phys. Rev. D* **65**, 022002 (2001).
5. Unruh, W. G. *Quantum Optics, Experimental Gravitation, and Measurement Theory* (Plenum, 1982).
6. Buonanno, A. & Chen, Y. Quantum noise in second generation, signal-recycled laser interferometric gravitational-wave detectors. *Phys. Rev. D* **64**, 042006 (2001).
7. Kwee, P., Miller, J., Isogai, T., Barsotti, L. & Evans, M. Decoherence and degradation of squeezed states in quantum filter cavities. *Phys. Rev. D* **90**, 062006 (2014).
8. Danilishin, S. et al. Creation of a quantum oscillator by classical control. Preprint at https://arxiv.org/abs/0809.2024 (2008).
9. Purdue, P. & Chen, Y. Practical speed meter designs for quantum nondemolition gravitational-wave interferometers. *Phys. Rev. D* **66**, 122004 (2002).
10. Møller, C. B. et al. Quantum back-action-evading measurement of motion in a negative mass reference frame. *Nature* **547**, 191–195 (2017).
11. Purdy, T. P., Peterson, R. W. & Regal, C. A. Observation of radiation pressure shot noise on a macroscopic object. *Science* **339**, 801–804 (2013).
12. Suh, J. et al. Mechanically detecting and avoiding the quantum fluctuations of a microwave field. *Science* **344**, 1262–1265 (2014).
13. Wilson, D. J. et al. Measurement-based control of a mechanical oscillator at its thermal decoherence rate. *Nature* **524**, 325–329 (2015).
14. Teufel, J., Lecocq, F. & Simmonds, R. Overwhelming thermomechanical motion with microwave radiation pressure shot noise. *Phys. Rev. Lett.* **116**, 013602 (2016).
15. Cripe, J. et al. Measurement of quantum back action in the audio band at room temperature. *Nature* **568**, 364–367 (2019).
16. Sudhir, V. et al. Quantum correlations of light from a room-temperature mechanical oscillator. *Phys. Rev. X* **7**, 031055 (2017).
17. Purdy, T. P., Grutter, K. E., Srinivasan, K. & Taylor, J. M. Quantum correlations from a room-temperature optomechanical cavity. *Science* **356**, 1265–1268 (2017).
18. Mason, D., Chen, J., Rossi, M., Tsaturyan, Y. & Schliesser, A. Continuous force and displacement measurement below the standard quantum limit. *Nat. Phys.* **15**, 745–749 (2019).
19. Tse, M. et al. Quantum-enhanced advanced LIGO detectors in the era of gravitational-wave astronomy. *Phys. Rev. Lett.* **123**, 231107 (2019).
20. Abbott, B. P. et al. Gw150914: the advanced LIGO detectors in the era of first discoveries. *Phys. Rev. Lett.* **116**, 131103 (2016).
21. Sun, L. et al. Characterization of systematic error in advanced LIGO calibration. Preprint at https://arxiv.org/abs/2005.02531 (2020).

Detector group of The LIGO Scientific Collaboration

J. Betzwieser[3], C. D. Blair[3], S. E. Dwyer[4], A. Effler[3], M. Evans[1], A. Fernandez-Galiana[1], P. Fritschel[1], V. V. Frolov[3], F. Matichard[1,5], D. E. McClelland[2], T. McRae[2], A. Mullavey[3], D. Sigg[4], B. J. J. Slagmolen[2], C. Whittle[1], A. Buikema[1], Y. Chen[6], T. R. Corbitt[7], R. Schnabel[8], R. Abbott[5], C. Adams[3], R. X. Adhikari[5], A. Ananyeva[5], S. Appert[5], K. Arai[5], J. S. Areeda[9], Y. Asali[10], S. M. Aston[3], C. Austin[7], A. M. Baer[11], M. Ball[12], S. W. Ballmer[13], S. Banagiri[14], D. Barker[4], J. Bartlett[4], B. K. Berger[15], D. Bhattacharjee[16], G. Billingsley[5], S. Biscans[1,5], R. M. Blair[4], N. Bode[17,18], P. Booker[17,18], R. Bork[5], A. Bramley[3], A. F. Brooks[5], D. D. Brown[19], C. Cahillane[5], K. C. Cannon[20], X. Chen[21], A. A. Ciobanu[19], F. Clara[4], S. J. Cooper[22], K. R. Corley[10], S. T. Countryman[10], P. B. Covas[23], D. C. Coyne[5], L. E. H. Datrier[24], D. Davis[13], C. Di Fronzo[22], K. L. Dooley[25,26], J. C. Driggers[4], P. Dupej[24], T. Etzel[5], T. M. Evans[3], J. Feicht[5], P. Fulda[27], M. Fyffe[3], J. A. Giaime[3,7], K. D. Giardina[3], P. Godwin[28], E. Goetz[7,16], S. Gras[1], C. Gray[4], R. Gray[24], A. C. Green[27], Anchal Gupta[5], E. K. Gustafson[5], R. Gustafson[29], J. Hanks[4], J. Hanson[3], T. Hardwick[7], R. K. Hasskew[3], M. C. Heintze[3], A. F. Helmling-Cornell[12], N. A. Holland[2], J. D. Jones[4], S. Kandhasamy[30], S. Karki[12], M. Kasprzack[5], K. Kawabe[4], P. J. King[4], J. S. Kissel[4], Rahul Kumar[4], M. Landry[4], B. B. Lane[1], B. Lantz[15], M. Laxen[3], Y. K. Lecoeuche[4], J. Leviton[29], J. Liu[17,18], M. Lormand[3], A. P. Lundgren[31], R. Macas[25], M. MacInnis[1], D. M. Macleod[25], G. L. Mansell[1,4], S. Márka[10], Z. Márka[10], D. V. Martynov[22], K. Mason[1], T. J. Massinger[1], R. McCarthy[4], S. McCormick[3], J. McIver[5], G. Mendell[4], K. Merfeld[12], E. L. Merilh[4], F. Meylahn[17,18], T. Mistry[32], R. Mittleman[1], G. Moreno[4], C. M. Mow-Lowry[22], S. Mozzon[31], T. J. N. Nelson[3], P. Nguyen[12], L. K. Nuttall[31], J. Oberling[4], Richard J. Oram[3], C. Osthelder[5], D. J. Ottaway[19], H. Overmier[3], J. R. Palamos[12], W. Parker[3,33], E. Payne[34], A. Pele[3], C. J. Perez[4], M. Pirello[4], H. Radkins[4], K. E. Ramirez[35], J. W. Richardson[5], K. Riles[29], N. A. Robertson[5,24], J. G. Rollins[5], C. L. Romel[4], J. H. Romie[3], M. P. Ross[36], K. Ryan[4], T. Sadecki[4], E. J. Sanchez[5], L. E. Sanchez[5], T. R. Saravanan[30], R. L. Savage[4], D. Schaetzl[5], R. M. S. Schofield[12], E. Schwartz[3], D. Sellers[3], T. Shaffer[4], J. R. Smith[9], S. Soni[7], B. Sorazu[24], A. P. Spencer[24], K. A. Strain[24], L. Sun[5], M. J. Szczepańczyk[27], M. Thomas[3], P. Thomas[4], K. A. Thorne[3], K. Toland[24], C. I. Torrie[5], G. Traylor[3], A. L. Urban[7], G. Vajente[5], G. Valdes[7], D. C. Vander-Hyde[13], P. J. Veitch[19], K. Venkateswara[36], G. Venugopalan[5], A. D. Viets[37], T. Vo[13], C. Vorvick[4], M. Wade[38], R. L. Ward[2], J. Warner[4], B. Weaver[4], R. Weiss[1], B. Willke[17,18], C. C. Wipf[5], L. Xiao[5], H. Yamamoto[5], Hang Yu[1], L. Zhang[5], M. E. Zucker[1,5] & J. Zweizig[5]

[3]LIGO Livingston Observatory, Livingston, LA, USA. [4]LIGO Hanford Observatory, Richland, WA, USA. [5]LIGO, California Institute of Technology, Pasadena, CA, USA. [6]Caltech CaRT, Pasadena, CA, USA. [7]Louisiana State University, Baton Rouge, LA, USA. [8]Universität Hamburg, Hamburg, Germany. [9]California State University Fullerton, Fullerton, CA, USA. [10]Columbia University, New York, NY, USA. [11]Christopher Newport University, Newport News, VA, USA. [12]University of Oregon, Eugene, OR, USA. [13]Syracuse University, Syracuse, NY, USA. [14]University of Minnesota, Minneapolis, MN, USA. [15]Stanford University, Stanford, CA, USA. [16]Missouri University of Science and Technology, Rolla, MO, USA. [17]Max Planck Institute for Gravitational Physics (Albert Einstein Institute), Hanover, Germany. [18]Leibniz Universität Hannover, Hanover, Germany. [19]OzGrav, University of Adelaide, Adelaide, South Australia, Australia. [20]RESCEU, University of Tokyo, Tokyo, Japan. [21]OzGrav, University of Western Australia, Crawley, Western Australia, Australia. [22]University of Birmingham, Birmingham, UK. [23]Universitat de les Illes Balears, IAC3—IEEC, Palma de Mallorca, Spain. [24]SUPA, University of Glasgow, Glasgow, UK. [25]Cardiff University, Cardiff, UK. [26]The University of Mississippi, University, MS, USA. [27]University of Florida, Gainesville, FL, USA. [28]The Pennsylvania State University, University Park, PA, USA. [29]University of Michigan, Ann Arbor, MI, USA. [30]Inter-University Centre for Astronomy and Astrophysics, Pune, India. [31]University of Portsmouth, Portsmouth, UK. [32]The University of Sheffield, Sheffield, UK. [33]Southern University and A&M College, Baton Rouge, LA, USA. [34]OzGrav, School of Physics and Astronomy, Monash University, Clayton, Victoria, Australia. [35]The University of Texas Rio Grande Valley, Brownsville, TX, USA. [36]University of Washington, Seattle, WA, USA. [37]Concordia University Wisconsin, Mequon, WI, USA. [38]Kenyon College, Gambier, OH, USA.

Methods

Extended interferometer model

The model curves presented in Figs. 2, 3 and Extended Data Figs. 1, 2 are calculated from the full coupled-cavity equations of ref. [6], which are exact and omit only effects from high-order transverse optical modes. The model provided by equations (1)–(5) represents an ideal interferometer with all cavities on resonance and no optical losses. Here we extend the model to consider the dominant experimental deviations from the ideal case, without the complexity of the exact equations. This extension includes imperfect input and output efficiency, as well as the additional frequency-dependent effect on the squeezing angle from the small, unintended phase shift within the signal-recycling cavity. For the parameters used in this study, the following model is accurate to 5% or better of the exact-model quantum power spectral density at frequencies between 10 Hz and 100 Hz.

The input and output efficiency of the interferometer are introduced using two new parameters, η_i and η_o, respectively. The input efficiency represents the total fractional coupling of optical power between the squeezer cavity and the interferometer, and the output efficiency is that from the interferometer to the GW readout. They must be considered separately owing to differences in their interaction with the QRPN, leading to the expressions:

$$\Delta x^2(\Omega) = S^*[1+\eta_o\mathcal{K}^2(\Omega)]\frac{\hbar c}{\eta_o 8k|G(\Omega)|^2 P_{arm}} \tag{6}$$

$$1-\eta_e = (1-\eta_i)+\frac{1}{1+\eta_o\mathcal{K}^2(\Omega)}(1-\eta_o) \tag{7}$$

$$S^*(\Omega,\phi,\psi) = \eta_e S(\Omega,\phi,\psi)+(1-\eta_e) \tag{8}$$

$$S(\Omega,\phi,\psi) = e^{-2r}\cos^2(\phi-\theta^*)+e^{2r}\sin^2(\phi-\theta^*) \tag{9}$$

$$\theta^* = \arctan[\mathcal{K}(\Omega)]+\frac{\Omega^2}{\gamma^2+\Omega^2}\psi \tag{10}$$

External output loss does not change the dark-port-to-arm-cavity optical-field transmissivity $G(\Omega)$, but it does modify the dark-port-to-readout transmissivity, lowering the sensing function to $2kG(\Omega)\sqrt{\eta_o P_{arm}}$. This leads to the η_o terms in equation (6), where the shot noise scales as $1/\eta_o$ but the QRPN term does not. The QRPN pertains to real motion, and its reduced influence on the optical quantum noise is compensated by the Δx calibration.

The frequency-dependent effective efficiency, η_e, accounts for the output loss $1-\eta_o$ not being able to affect the real motion of the masses owing to radiation pressure, while the squeezed state is degraded by both input and output losses. The form of equation (7) reflects the relationship of the input, output and effective losses rather than efficiencies, and it is accurate for small losses.

The total squeezing angle shift due to the signal-recycling cavity is encoded in the parameter ψ. It appears alongside the ponderomotive effect on the squeezing angle in equation (10), except it accumulates through the cavity pole transition. This formulation is accurate for a small physical round-trip phase shift (detuning), ξ, of the interferometer signal cavity. This physical detuning results in a cavity-induced squeezing phase shift of $\psi = 10.7\xi$ calculated for the LIGO Livingston mirror parameters. Notably absent from this non-ideal model, but present in ref. [6], is the interaction between radiation pressure and the signal-recycling cavity detuning, $\xi \neq 0$, which is typically labelled an 'optical spring'. This interaction is accounted for in the calibration and exact-model curves included in our plots, but at this ξ and ψ it is not significant for the analysis. We note that the above non-ideal model is accurate to 1% in the zero-detuning case $\psi = \xi = 0$ versus a 5% discrepancy when detuning is included. Whereas strong optical springs are an alternative method of achieving sub-SQL quantum noise sensitivity, this indicates that the spring contribution is weak compared to the injected squeezing.

Measurement sequence

The data shown in Fig. 2 were taken over a 5-h period on the advanced LIGO detector. To avoid variations of classical noise and calibration, the interferometer power is held constant across all measurements. To minimize the statistical error, the majority of the measurement time is spent in the two modes plotted: three 30-min 'reference' segments with the squeezer disabled, alternating with three 30-min segments with squeezing at $\phi = 35°$. Each reference segment is followed by a squeezing segment, alternating three times to establish that the classical noise contribution is constant across the total duration. The remaining time is split across nine additional segments at varying input squeezing angles, and the final segment is a fourth reference without squeezing.

The parameters describing the status of the interferometer and squeezer during the experiment are listed in Extended Data Table 1 with uncertainties. These are also the values used in the modelling of the quantum noise calculation. Immediately before the 5-h dataset, the nonlinear parameter of the squeezer was measured to calculate r. The squeezing angle is determined ultimately through a model fit, but it agrees with our knowledge of the nonlinear conversion from the demodulation angle of the coherent control field to the observed squeezing angle and the settings during the shot-noise squeezing ($\phi = 0°$) and antisqueezing ($\phi = 90°$) datasets. The frequency-dependent contributions of the squeezing and arm-power modelling uncertainties are shown in Extended Data Fig. 1, and they do not strongly influence the model at the sub-SQL dip.

Extended Data figures

Extended Data Fig. 1 shows a variation of Fig. 2 spanning a wider frequency range. The figure includes the frequency-dependent uncertainties of equation (12) in its model curves and subtracted quantum noise plots.

Extended Data Fig. 2 shows a measurement (top) and a model (bottom) of the squeezing term $S^*(\Omega,\phi,\psi)$ of the augmented model. The quantum noise spectrum at ten additional ϕ values is determined by subtracting the classical noise contribution (previously established through the reference measurement) from the measured displacement spectrum at each ϕ. Each inferred quantum noise spectrum is then divided by the modelled quantum noise spectrum without injected squeezing (blue trace in Fig. 2) to obtain the observed squeezing term $S^*(\Omega,\phi,\psi)$. The dashed lines indicate cross-sections in other figures: the green line corresponds to $\phi = 35°$ in Fig. 2, and the magenta, navy and brown lines to the angles $\phi = 7°$, 24° and 46° shown in Fig. 3.

Uncertainty analysis for subtraction

Figure 2 shows that quantum noise accounts for only 28% of the total interferometer noise power at 40 Hz. For this reason, classical noises must be subtracted to reveal the quantum noise-limited displacement sensitivity. The interferometer is a complex instrument with such environmental sensitivity that the following considerations must be addressed to validate the subtraction. First, the fiducial quantum noise model of the reference dataset and the parameters that it relies on must be established, and the data must be calibrated. Second, the classical noise established for the reference operating mode must be representative of the classical noise during the squeezing operation. In particular, the classical noise during the reference period must

not be higher than that during squeezing, which would bias our inference to underestimate the quantum noise contribution during squeezing.

To describe how uncertainty propagates through the subtraction in our measured quantum noise curves, we consider uncertainties in four sources: (a) the calibration, (b) quantum noise models, (c) statistical noise and (d) non-stationary changes in the noise contributions. D_r, D_s, M_r and M_s denote the frequency-dependent data and model spectral densities for the reference and squeezing operating cases, respectively. For our analysis, we use and plot the full coupled-cavity equations[4,6] including all losses and optical spring effects, but reiterate that the deviation between the exact model and the simplified model of equations (6)–(10) is small for our operating parameters. The post-subtraction inferred quantum noise is given as Q in the expression:

$$Q(\Omega) = D_s(\Omega) - [D_r(\Omega) - M_r(\Omega)] \tag{11}$$

The relative error of the post-subtraction squeezed quantum noise is given by δQ and is composed of the quadrature sum of relative errors due to: the optical-sensitivity calibration, δG; the servo loop calibration, δC; the modelling uncertainty, δM_r; statistical fluctuations, δD_r and δD_s; and relative stationarity uncertainty terms, δN_t and δN_m. All of these uncertainties are frequency-dependent, but the full functional forms are omitted for brevity. These components, which are defined in the following section, contribute to the expression:

$$\begin{aligned}\delta Q^2 = \delta G^2 + \frac{1}{Q^2}[&M_r^2\delta M_r^2 + (D_r - D_s)^2\delta C^2 \\ &+ D_r^2\delta D_r^2 + D_s^2\delta D_s^2 \\ &+ (D_r - M_r)^2(\delta N_t^2 + \delta N_m^2)].\end{aligned} \tag{12}$$

The lines of the above equation represent terms with different magnitudes of scaling terms. Given that $Q \approx M_s \approx D_r - D_s$, the top line for the calibration and model error has terms with order-1 coefficients, indicating that the relative errors quoted in the main text remain small for the comparison to the dip model. The lower two lines of equation (12) show that the relative statistical fluctuations and stationarity uncertainties are magnified by the ratio V between the total classical power spectral density D_r and the quantum noise Q to the squeezed quantum power spectral density, which is approximately $V = 7.2$ at 40 Hz.

Calibration and modelling uncertainty

The first line of equation (12) includes the calibration and unsqueezed reference quantum noise model uncertainty terms, δG, δC and δM_r. The LIGO online calibration system determines the optical sensing function $2kG(\Omega)\sqrt{\eta_o P_{arm}}$, which affects both the model and the calibration uncertainties. To prevent double-counting in the incoherent sum, this optical gain has been isolated to the factor δG and should not be considered in δC or δM_r. The sensing function is monitored continuously by injecting displacement signals at several frequencies. Some of these appear as narrow lines in the measured spectra of Fig. 2. From these continuous injections, the bandwidth γ and the product $\eta_o P_{arm}$ are determined. In addition, parameters related to the optical spring are measured[22], but primarily affect the sensing function at frequencies <10 Hz for the measured detuning ξ, ψ. Additional lines monitor the Δx servo loop actuators to apply the frequency-dependent correction for the servo closed-loop response, which is contained in δC. The quoted frequency-dependent calibration uncertainty is the incoherent sum $\sqrt{\delta G^2 + \delta C^2}$, and error bars in Extended Data Fig. 1 include the frequency dependence.

Having factored δG out of δM_r, any error in subtracting the classical noise estimate between the reference data and the model can only arise from estimating the shot-noise and QRPN components represented by the term $g[1 + \eta_o \mathcal{K}^2(\Omega)]$. Here, g is a scale factor relating the readout power to the optical field. It is unknown because the calibration system exports its sensing function in an end-to-end fashion with the photodetectors in arbitrary voltage digitization units; however, g may be well estimated using a cross-correlation method detailed below. The remaining $g\eta_o \mathcal{K}^2(\Omega)$ contribution may be estimated from the factors $|G(\Omega)|^2\sqrt{P_{arm}}$. Independent measurements establish the quoted arm power to be $P_{arm} = 200 \pm 10$ kW; this, combined with the optical sensing gain calibration, allows us to determine the output efficiency η_o. The squeezing level at high frequencies is determined by r and $\eta_o\eta_i$ (see equations (7), (8)) and, using the extended datasets with $\phi = 0°$, the input efficiency η_i may be determined from the observed readout squeezing level.

The following cross-correlation method[22] is used to determine the factor g that relates the arbitrary experimental photodetector units back to the physical optical-field units. Two photodetectors are located at the readout port of the LIGO interferometer (see Fig. 1). When squeezing is not injected, the shot noise and the readout electronics noise (that is, dark noise) are uncorrelated between the two photodetectors, whereas the QRPN and all of the classical noises are correlated. If the cross-correlation and dark noise are subtracted from the total noise power for the reference dataset, then only the shot noise remains, which is calibrated to the displacement. This precisely determines the optical sensing gain in physical units, up to the uncertainty δG. The dark noise, also incoherent between the detectors, is only 1% of the shot-noise power and so contributes negligibly to the uncertainty in this subtraction.

Statistical uncertainty

The statistical uncertainty arises because the fluctuations that are intrinsic to noise also limit our ability to estimate it. With a total measurement time of T_i for a given dataset i, and a bin width of $\Delta F = 0.5$ Hz in the spectral density calculation, the relative statistical uncertainty of the inferred quantum noise power is $\delta D_i = (ET_i\Delta F)^{-1/2}$, with E the statistical efficiency accounting for the spectral estimation method. For the median method detailed below, we determine through numerical experiments on white noise that $E = 1.0$ for single-bin error bars. The bin–bin covariance due to the apodization window results in $E = 60\%$ when averaging multiple adjacent data points. The total statistical uncertainty of 8% includes both datasets δD_r and δD_s and their scaling by V in equation (12).

Measuring noise stationarity

Here we describe and characterize the terms δN_t, δN_m in the uncertainty budget of equation (12). We define these terms together as the stationarity uncertainty, and they are intended to quantify potential variations between the classical noise power, as estimated from the unsqueezed reference dataset, and the classical noise power that is actually present in the squeezing measurements. Under the presupposition that the models M_r and M_s are perfect and the statistical noise is small, these uncertainties are defined as the relative difference $D_s - M_s \equiv (D_r - M_r)(1 + \delta N_t + \delta N_m)$. The two terms are distinguished as the changes to the classical noise that arise from variations in time, δN_t, and from switching the physical operating mode between the reference and squeezing, δN_m.

Stationarity uncertainty mitigation

The time variation contribution to non-stationarity, δN_t, is mitigated both through the spectral density estimation method and the use of three alternating segments for the reference and squeezed data. The aim of the alternating segments is for the operating mode to switch on a timescale shorter than the environmental variation. The environmental timescale is not known or even well defined, so instead the discontiguous segments of reference time are compared, setting a limit to the non-stationarity of the squeezing segment between them. This is done likewise for the squeezing segments surrounding a reference

segment. We define a metric for the relative non-stationarity between two such discontiguous segments to be:

$$\mathcal{N}_{ij} = 2\frac{D_i - D_j}{D_i + D_j}. \quad (13)$$

Each pair of datasets is used to make an estimate of the noise contribution varying at and below the separation timescale of the datasets; here, 1 h. The estimates $\mathcal{N}_{ij}$ are limited by the statistical error of the constituent reference and squeezing datasets, denoted as $\mathcal{N}_{\mathrm{R}ij}$ and $\mathcal{N}_{\mathrm{S}ij}$, respectively, and they are shown in Extended Data Fig. 3. Because each pair comprises only a fraction of its full dataset, multiple estimates are combined to reduce the statistical uncertainty.

$$\mathcal{N}_{\Sigma}^2 = \frac{1}{6}(\mathcal{N}_{\mathrm{R}12}^2 + \mathcal{N}_{\mathrm{R}23}^2 + \mathcal{N}_{\mathrm{R}31}^2 + \mathcal{N}_{\mathrm{S}12}^2 + \mathcal{N}_{\mathrm{S}23}^2 + \mathcal{N}_{\mathrm{S}31}^2). \quad (14)$$

Finally, these metrics must be related to the stationarity term δN_t. The averaged non-stationary power $\mathcal{N}_{\Sigma}^2$ represents an estimate of the time-varying contribution between adjacent reference and squeezing segments, of which there are three. For many such segments, assuming random fluctuations to the environmental noise level at the alternation timescale, the contributions add in quadrature to give $\delta N_t^2 \lesssim \mathcal{N}_{\Sigma}^2/3$. We then propagate the statistical noise limits for segments with one-third of the length of the total reference time T. This arrives at the statistical limit to our stationarity uncertainty of $\delta N_t \approx \sqrt{2}\,(ET\Delta F)^{-1/2}$. Because the total squeezing data time is also T, our limit to the time variation contribution to non-stationarity is evaluated to be the same as the total statistical uncertainty from both the squeezed and unsqueezed datasets, $\delta N_t^2 \approx \delta D_{\mathrm{r}}^2 + \delta D_{\mathrm{s}}^2$. In addition to the individual pairs, Extended Data Fig. 3 shows the combined estimate $\mathcal{N}_{\Sigma}^2$.

The operating mode variation component δN_m of non-stationary noise is constrained by the following considerations. The first is that it is quantitatively constrained by the data at the additional squeezing angles depicted in Fig. 3 and Extended Data Fig. 2. There, the same classical noise estimate is subtracted and the model curves maintain their agreement with the inferred quantum noise at alternate squeezing angles. Those datasets, however, have limited statistical bounds owing to their short duration. The term δN_m may be considered small for the following physical reasons. The primary reason is that during the time without squeezing, the optical path is not changed, and only the optical parametric oscillator cavity[19] which produces the squeezed states is operated off resonance to stop its nonlinear parametric interaction. This means that environmental scatter noise—the very-low-power light leaking from the interferometer to the squeezer system—does not impinge on different scattering surfaces between the two modes. In the event that such scatter does matter, the fourth reference taken at the end of the entire measurement period uses an in-vacuum beam diverter to block the path to the squeezer. Testing that fourth reference against the other three through the $\mathcal{N}_{ij}$ method shows no substantial changes to the classical noise.

If the classical noise does change from the switch to squeezing, we argue that the addition of the nonlinear parametric interaction from the squeezer to this scattered light is more likely to increase the noise only during the squeezing segments. This implies that the measurement should not be biased low and will not overestimate how much we have surpassed the SQL. Indeed, the few data points in Fig. 2 and Extended Data Fig. 1 that exceed the model beyond the statistical fluctuations may be due to such a squeezer-specific noise source. We attribute the minimal classical noise contribution to the use of a travelling-wave optical parametric oscillator cavity, the in-vacuum suspended layout and coherent control implementation[19].

Spectral density estimation

To mitigate the non-stationary noise power contributions, a statistically robust median-based computation method is used to calculate the sampled power spectral density. Based on the above considerations, we claim that the classical noise is established to be stationary in these datasets; however, it is known from astrophysical analysis that these complex detectors have intermittent time-resolved glitches and artefacts of varying strength. Intervals of excess noise are nontrivial to identify owing to the inherently random nature of noise, and time-resolved noise power vetoes can introduce selection bias. We use the Welch–Bartlett overlap method to estimate the power spectral density with no selection vetoes. Instead, rather than averaging the individual spectra independently at each frequency, the sample median at each frequency is taken. This generates a bin-by-bin median strain spectral power density.

Initially, the entire period for a given spectral density estimate is split into N 2-s segments, where each segment overlaps the segment before it by 50%, implementing the Welch method. For each segment, the time series is linearly detrended and a Hann window is applied; then, the time series is converted to a displacement spectrum using a Fourier transform. The collection of segments gives N estimates of the power density in each frequency bin, each of which nominally follows a χ^2 distribution on two variables (the real and imaginary parts of the Fourier transform), but the distribution has an extended tail due to glitches and transients of the detector. The median is picked for each frequency bin, and then a computed scale factor is applied to convert the distribution median to the mean noise power. This technique is unbiased for stationary noise and greatly improves the robustness to glitches and non-stationary contributions, without selection bias from time-domain band-limited noise vetoes. The downside is that the statistical efficiency is approximately $\sqrt{2}$ worse than the typical Welch method for a given spectrum-averaging time.

Data availability

Source data for Figs. 2, 3, Extended Data Figs. 1–3 and other data pertaining to this study are available from the corresponding authors upon reasonable request.

22. Kiwamu, I. Time domain implementation of dcpd cross correlation. *Technical Note* T1700131 (LIGO Virgo, 2017); https://dcc.ligo.org/LIGO-T1700131/public.

Acknowledgements LIGO was constructed by the California Institute of Technology and the Massachusetts Institute of Technology with funding from the National Science Foundation, and operates under Cooperative Agreement number PHY-1764464. Advanced LIGO was built under grant number PHY-0823459. The authors gratefully acknowledge the support of the Australian Research Council under the ARC Centre of Excellence for Gravitational Wave Discovery grant number CE170100004, Linkage Infrastructure, Equipment and Facilities grant number LE170100217 and Discovery Early Career Award number DE190100437; the National Science Foundation Graduate Research Fellowship under grant number 1122374; the Science and Technology Facilities Council of the United Kingdom; and the LIGO Scientific Collaboration Fellows programme.

Author contributions The measurements presented in this paper were performed with the 4-km detector at the LIGO Livingston Observatory using a novel squeezed light source. Haocun Yu performed all of the measurements. Haocun Yu and L.M. carried out the analysis of the data. M. Tse, Haocun Yu and N.K. built and commissioned the squeezed-light sources. L.B. led the squeezed-light upgrade of the LIGO detectors, involving contributions from a large number of people within the LIGO Laboratory, the Australian National University and other members of the LIGO Scientific Collaboration. N.M. led the experimental campaign to measure sub-SQL quantum noise in the Advanced LIGO detector. Haocun Yu, L.M., M. Tse, L.B. and N.M. contributed directly to the preparation of the manuscript.

Competing interests The authors declare no competing interests.

Additional information

Correspondence and requests for materials should be addressed to Haocun Yu or L.M.

Peer review information *Nature* thanks Albert Schliesser, Valeria Sequino and Kentaro Somiya for their contribution to the peer review of this work.

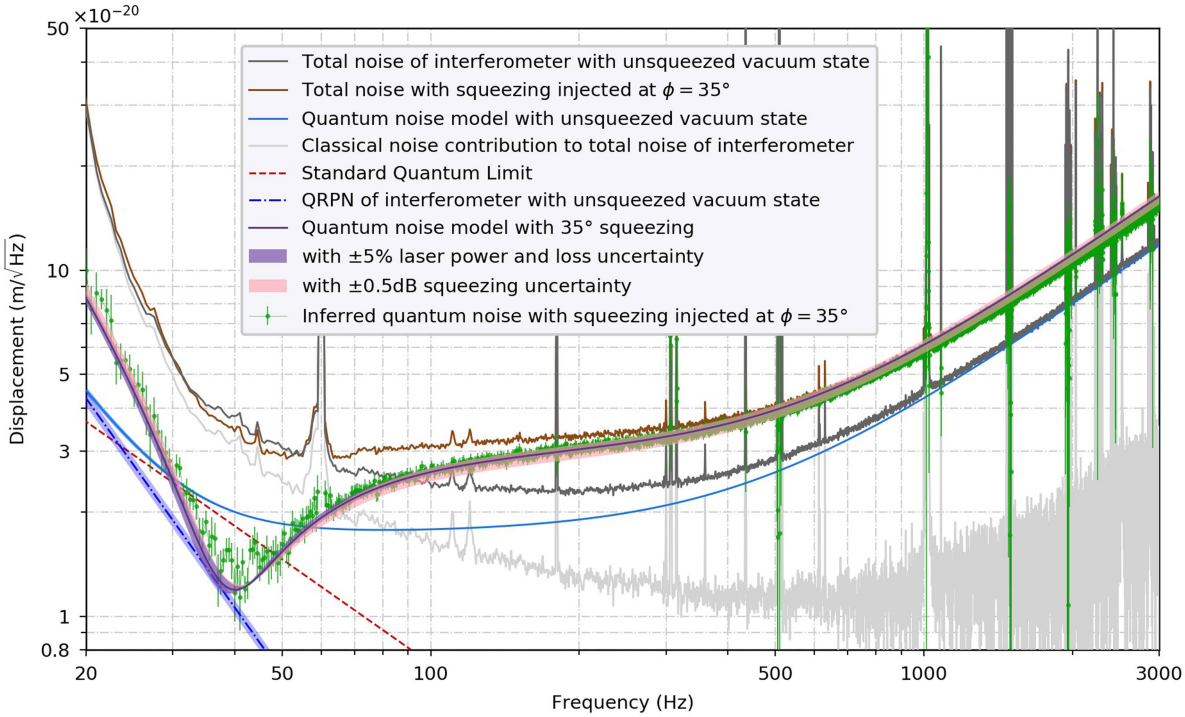

Extended Data Fig. 1 | Spectral density measurements revealing sub-SQL quantum noise of the interferometer with uncertainties. The black and brown traces show the measured total noise level of the interferometer with the unsqueezed vacuum state (the reference) and injected squeezing at 35°, respectively. The grey curve shows the classical noise contribution to the total noise of the interferometer, which is independent of the squeezer state. The solid blue curve shows the quantum noise model and includes the 5% uncertainty in the arm power, compensated by the output optical loss to maintain the calibrated sensing function. The inferred quantum noise (green curve) and error bars include all uncertainty terms present in equation (12), as estimated in Methods, including the frequency dependence. The quantum noise model with 35° squeezing (purple line) is shown with the 5% arm power uncertainty (purple shading) and the 0.5-dB uncertainty of the squeezing generated by the squeezer (pink shading). The free-mass SQL is shown by the dashed red line, and the pure QRPN contribution of the interferometer with the unsqueezed vacuum state is shown by the dashed blue line and includes the uncertainty in the arm power.

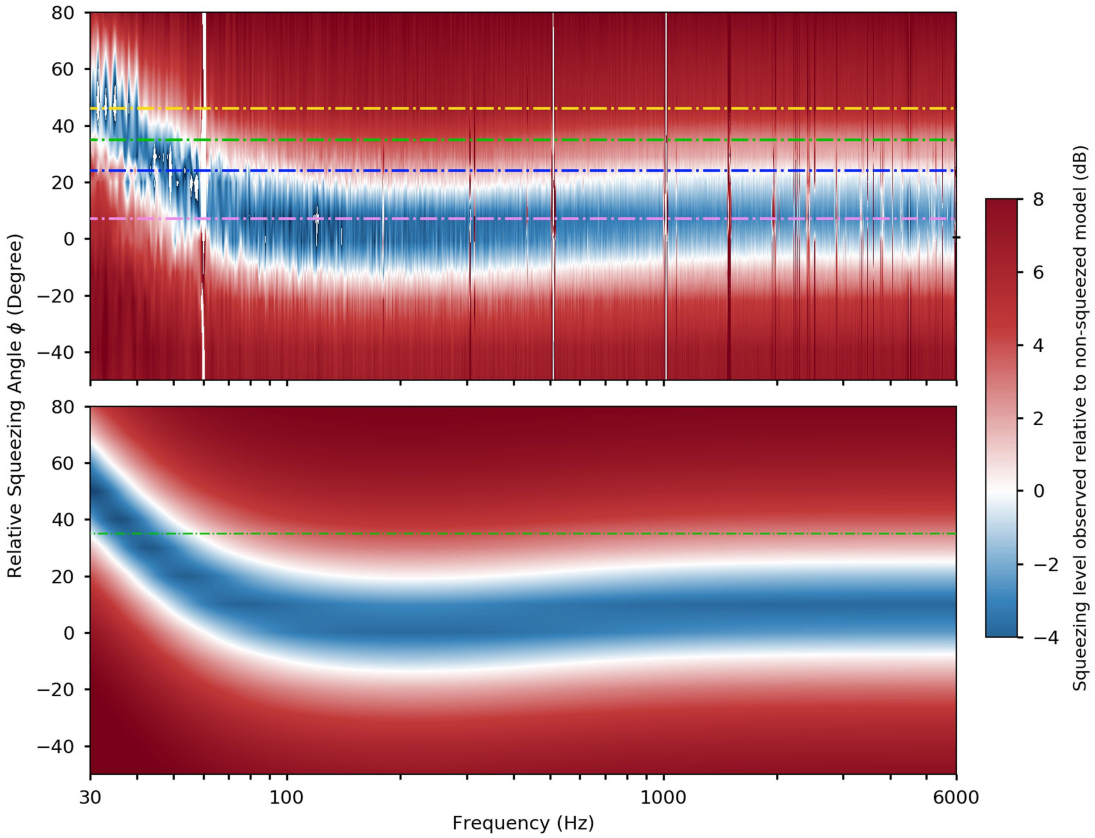

Extended Data Fig. 2 | Squeezing level of the interferometer over the full range of squeezing angles. Contour plot of squeezing level $S^*(\phi, \theta, \psi)$ detected in the interferometer as a function of the frequency and squeezing angle ϕ (top) and the corresponding theoretical model (bottom). The dashed lines indicate cross-sections in other figures. The green dashed line shows $\phi = 35°$ in Fig. 2, and the magenta, navy and orange lines correspond to the angles shown in Fig. 3.

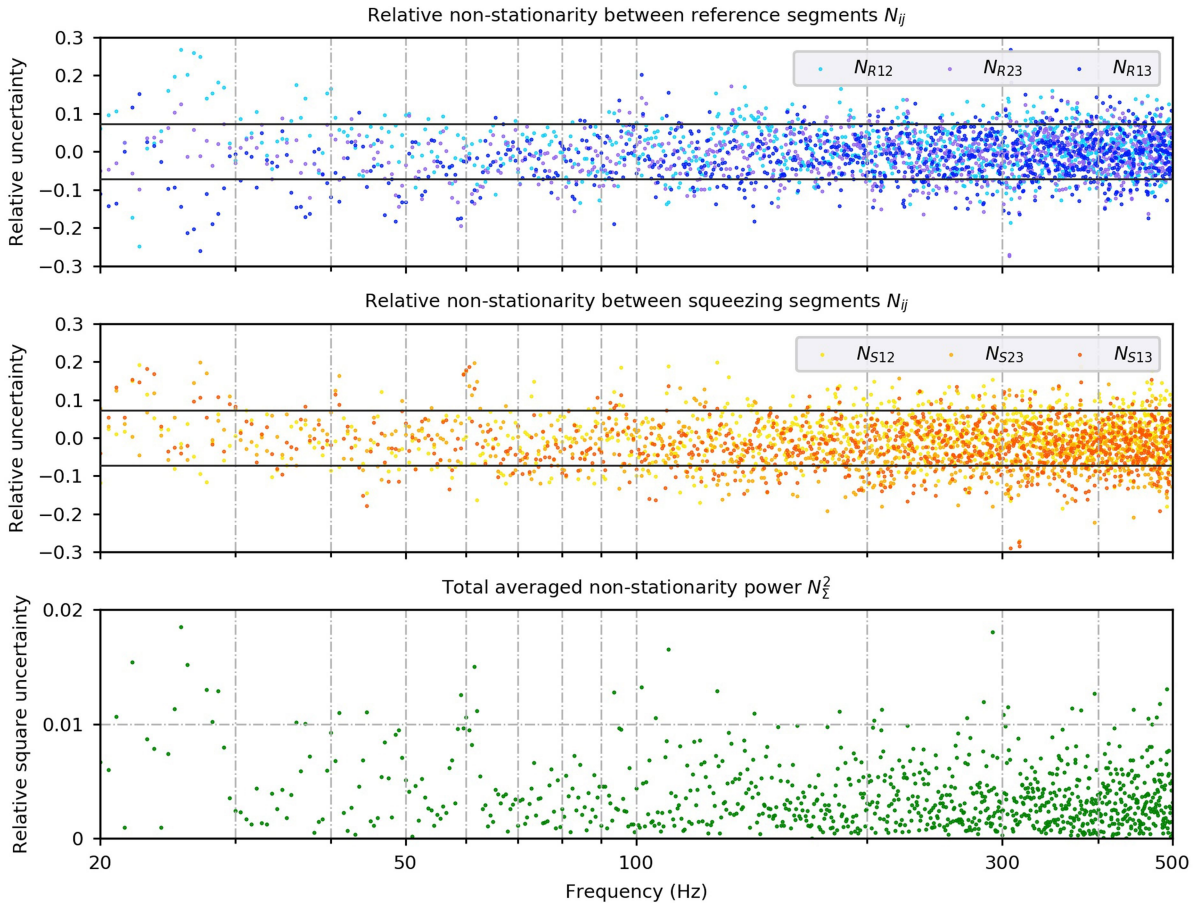

Extended Data Fig. 3 | Individual and combined estimates of non-stationary noise between measurement segments. The two upper plots show the relative time variation of noise between each pair of reference and squeezing measurement segments, respectively. The black lines show 2σ or a 95% confidence level. The bottom plot shows the combined non-stationary power defined by equation (14).

Extended Data Table 1 | Interferometer and squeezer parameters used for modelling the Advanced LIGO detector in Livingston

Interferometer Parameter	Value
Laser power in the arm cavity (P_{arm})	200±10 kW
Optical loss before interferometer ($1-\eta_i$)	17.2%
Optical loss after interferometer ($1-\eta_o$)	17.4%
SRM phase detuning (ξ)	15 mrad

Squeezer Parameter	Value
Measured OPO nonlinear gain	4.4±0.1
Squeezing ideally generated by OPO (e^{-2r})	9.8±0.15 dB
Squeezer phase noise ($\delta\phi$)	0-50 mrad
Squeezing quadrature rotation angle (ϕ)	35°
Max phase squeezing in interferometer	3.3 dB
Max phase anti-squeezing in interferometer	7.7 dB